Differentiating oral lesions in different carcinogenesis stages with optical coherence tomography

Meng-Tsan Tsai
Cheng-Kuang Lee
Hsiang-Chieh Lee
National Taiwan University
Institute of Photonics and Optoelectronics
1 Roosevelt Road, Section 4
Taipei, 10617
Taiwan

Hsin-Ming Chen
Chun-Pin Chiang
National Taiwan University
School of Dentistry
1 Roosevelt Road, Section 4
Taipei, 10048
Taiwan

Yih-Ming Wang
National Taiwan University
Institute of Photonics and Optoelectronics
1 Roosevelt Road, Section 4
Taipei, 10617
Taiwan

Chih-Chung Yang
National Taiwan University
Institute of Photonics and Optoelectronics and
   Department of Electrical Engineering
1 Roosevelt Road, Section 4
Taipei, 10617
Taiwan

Abstract. A swept-source optical coherence tomography (SS-OCT) system is used to clinically scan oral lesions in different oral carcinogenesis stages, including normal oral mucosa control, mild dysplasia (MiD), moderate dysplasia (MoD), early-stage squamous cell carcinoma (ES-SCC), and well-developed SCC (WD-SCC), for diagnosis purpose. On the basis of the analyses of the SS-OCT images, the stages of dysplasia (MiD and MoD), and SCC (ES-SCC and WD-SCC) can be differentiated from normal control by evaluating the depth-dependent standard deviation (SD) values of lateral variations. In the dysplasia stage, the boundary between the epithelium (EP) and lamina propria (LP) layers can still be identified and the EP layer becomes significantly thicker than that of normal control. Also, in a certain range of the EP layer above the EP/LP boundary, the SD value becomes larger than a certain percentage of the maximum level, which is observed around the EP/LP boundary. On the other hand, in the ES-SCC and WD-SCC stages, the EP/LP boundary disappears. Because of the higher density of connective tissue papillae in the ES-SCC stage, the SD values of the slowly varying lateral scan profiles in the ES-SCC samples are significantly larger than those in the WD-SCC sample. Also, ES-SCC can be differentiated from WD-SCC by comparing the exponential decay constants of averaged A-mode scan profiles. Because of the higher tissue absorption in the WD-SCC lesion, the decay constants in the WD-SCC samples are significantly higher than those in the ES-SCC samples. © *2009 Society of Photo-Optical Instrumentation Engineers.*
 [DOI: 10.1117/1.3200936]

1 Introduction

Squamous cell carcinoma (SCC) is the most common cancer type in the oral cavity.[1–5] It usually evolves from oral mucosal lesions with benign epithelial hyperplasia (EH) and mild dysplasia (MiD). EH and MiD are reversible lesions. Such patients may return to healthy if they stop their harmful oral habits. However, if an oral lesion evolves into the moderate dysplasia (MoD) or severe dysplasia stages, it will usually develop further into an early-stage SCC (ES-SCC) and then a well-developed SCC (WD-SCC) if an effective medical action is not taken. In the precancerous stage, dysplastic cells are present only in the epithelium (EP) layer. These precancerous lesions are classified into MiD, MoD, and severe dysplasia, when enough dysplastic cells are found in the basal one-third, in the basal two-thirds, or in more than the basal two-thirds but not the complete EP layer, respectively. When dysplastic cells occupy the whole EP layer, the lesion is called carcinoma *in situ*. In the early stage of SCC, cancer cells destroy the basement membrane [i.e., the boundary between the EP

and lamina propria (LP) layers] form nests, and invade into the underlying LP layer. Histopathologically, oral WD-SCCs can be further classified into well-, moderately, and poorly differentiated SCC, depending on the differentiation of cancer cells. The well-differentiated SCC is the most common type of oral SCC and constitutes approximately 80–90% of total oral SCC cases.

In clinical practice, most oral precancer patients begin to visit to the clinic when their oral lesions are in the stages of MiD (reversible) and MoD (irreversible) because the oral symptoms and signs become obvious in these stages. Therefore, the differentiation between different oral dysplasia stages or between oral dysplasia and oral SCC stages is important in an oral disease clinic. Conventionally, oral lesions in different carcinogenesis stages can be confirmed by a biopsy. However, a noninvasive imaging technique, such as optical coherence tomography (OCT),[6–9] is preferred if it can be used for effectively diagnosing an oral lesion and differentiating the different stages of oral carcinogenesis. The OCT technique has been widely used for diagnosing various oral diseases.[10–23] For diagnosing oral cancer lesion, three effec-


Address all correspondence to: C. C. Yang, Institute of Photonics and Optoelectronics, National Taiwan University, 1, Roosevelt Road, Section 4, Taipei, 10617 Taiwan. E-mail: ccy@cc.ee.ntu.edu.tw

tive diagnosis indicators have been built based on the clinical oral cavity scanning of a swept-source OCT (SS-OCT) system.[23] The three indicators include the EP thickness, the standard deviation (SD) of an A-mode scan intensity profile in the EP layer, and the decay constant of the spatial-frequency spectrum of the A-mode scan profile. In a lesion, usually the EP thickness becomes larger if the boundary between the EP and LP layers can still be identified. Also, the SD becomes larger and the aforementioned decay constant becomes smaller. The EP thickness and A-mode scan SD in the LP layer can also be used as the effective indicators for diagnosing oral submucous fibrosis that is a precancerous condition with a high malignant transformation potential in patients with an *areca quid* chewing habit.[24,25]

In this paper, the SD of OCT signal along the lateral dimension and the exponential decay behavior of an A-mode scan profile are analyzed based on the clinical scans of patients with an SS-OCT system for differentiating oral lesions in different carcinogenesis stages. By plotting the depth-dependent lateral-scan SD variation, one can see the increasing range of enlarged SD value in the EP layer as a lesion develops from the condition of normal into MiD and then into MoD. Also, due to the higher density of connective tissue papilla (CTP) in the stage of ES-SCC, compared to that of WD-SCC, the slowing-varying lateral intensity profile fluctuates more strongly in an ES-SCC sample than that in a WD-SCC sample. Meanwhile, because the stronger light absorption of oral tissue in the WD-SCC stage, the A-mode scan profile decays faster in a WD-SCC sample, when compared to an ES-SCC sample. These two features can be used for differentiating ES-SCC from WD-SCC. In Sec. 2 the specifications and operation conditions of the SS-OCT system we used are discussed. Also, the samples used for this study are described. The histology images of oral lesions in different carcinogenesis stages are demonstrated and discussed in Sec. 3. Then, the corresponding SS-OCT results are shown and analyzed for building effective diagnosis indicators. Those for the differentiations between samples of normal control, MiD, and MoD are presented in Sec. 4. Those for differentiating ES-SCC from WD-SCC are presented in Sec. 5. Finally, conclusions are drawn in Sec. 6.

2 OCT System and Sample Preparation

The layout of the portable SS-OCT system and its operation specifications used in the hospital for clinical scanning has been described in an earlier publication of the same group.[23] A sweeping-frequency laser (Santec) of 110 nm in sweeping spectral range and 1310 nm in central wavelength is used as the light source, which can provide 6 mW in output power and 20 kHz in sweep rate. The light source is connected to a Mach–Zehnder interferometer consisting of two couplers and two circulators. The interference fringe signal is detected by a balanced photodectector (PDB150C, Thorlabs) and sampled by a high-speed digitizer (PXI-5122, National Instrument). The laser power incident onto the tissue sample is ~1.5 mW. The achieved SS-OCT system sensitivity and axial resolution in free space are 103 dB and 8 μm (~6 μm in tissue) at the depth of 1 mm, respectively. In the sample arm, the lateral scanning is implemented with a handheld probe consisting of a linear stepping motor (Haydon), which is used to achieve a
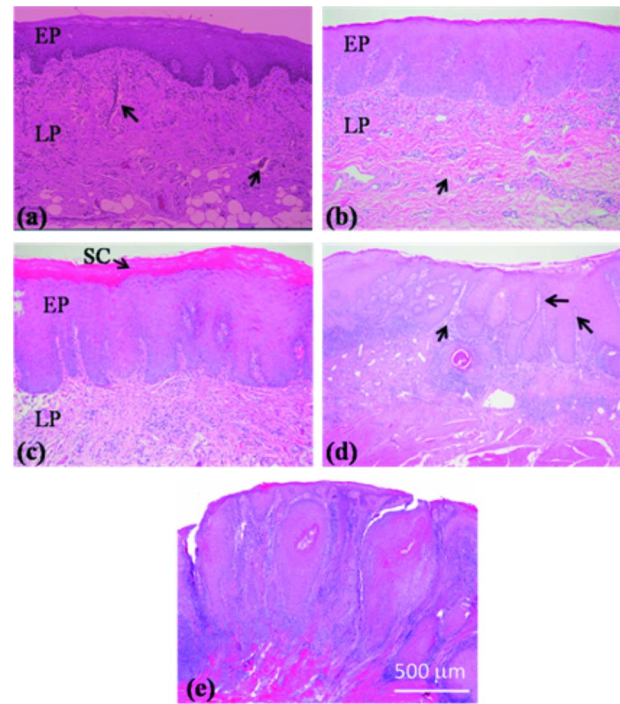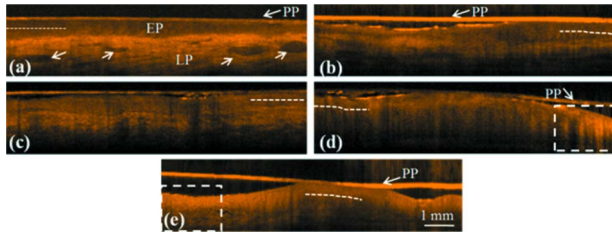

Fig. 1 Typical histology images of the (a) normal control, (b) MiD, (c) MoD, (d) ES-SCC, and (e) WD-SCC samples. The normal control image is taken from the normal oral mucosa of one of the patients.

scanning speed of 10 cm/s and a 1-cm scanning length. In clinical application, the whole probe is wrapped by a plastic plate to protect the optical components inside the probe. After the scanning of a patient, the wrapped plastic plate is discarded and the whole probe is sterilized with 70% ethanol. The lateral resolution of SS-OCT scanning is 15 μm. With this SS-OCT system, an image frame consisting of 2000 A-mode scans can be acquired within 0.1 s.

For building effective diagnosis indicators, we analyze the SS-OCT scanning images of four MiD, four MoD, four ES-SCC, and four WD-SCC lesions at the buccal mucosa of patients. Biopsy of the SS-OCT scanned oral lesion site is performed and histology images of the biopsy specimens are acquired for confirming the pathological diagnoses of the lesions. For comparison of scanning images, an SS-OCT image is obtained from the normal buccal mucosa of a healthy volunteer and used as the normal control sample. Also, a histology image of the normal buccal mucosa of a patient is used as the normal control sample for histological comparison.

3 Different Stages of Cancerous Lesion

Figures 1(a)–1(e) show the typical histology images of the normal control, MiD, MoD, ES-SCC, and WD-SCC samples, respectively. In the normal control image [Fig. 1(a)], the EP and LP layers can be clearly differentiated and two blood vessels (indicated by black arrows) can also be seen in the LP layer. In the MiD image [Fig. 1(b)], the EP layer is thickened, dysplastic cells are found in the lower one-third of the EP, and there is an increase in collagen deposition (indicated by the arrow) in the LP layer. In the MoD image [Fig. 1(c)], a thick stratum corneum (SC) layer is found on the EP surface, the

Fig. 2 SS-OCT scanned images of the (a) normal control and biopsied oral (b) MiD, (c) MoD, (d) ES-SCC, and (e) WD-SCC lesions whose histology images are shown in Figs. 1(a)–1(e). The normal control image in (a) is taken from a healthy volunteer.

EP layer becomes even thicker, and there are dysplastic and dyskeratotic cells found in the lower two-thirds of the EP layer. In the ES-SCC image [Fig. 1(d)], invaded cancer cell nests are scattered in the upper LP; this creates several slitlike CTPs among epithelial ridges or among cancer cell nests (exemplified by the three arrows). Finally, in the image of WD-SCC [Fig. 1(e)], many well-formed cancer cell nests are found. In addition, there is a prominent lymphocytic infiltrate in the stromal connective tissues among cancer cell nests.

4 Indicators for the Differentiation between Different Dysplasia Stages

Figures 2(b)–2(e) show the corresponding SS-OCT scanned images of the biopsied oral lesions whose histology images are shown in Figs. 1(b)–1(e). In the normal control image of Fig. 2(a), the boundary between the EP and LP layers is quite clear. The slitlike dark images in the LP layer, as exemplified
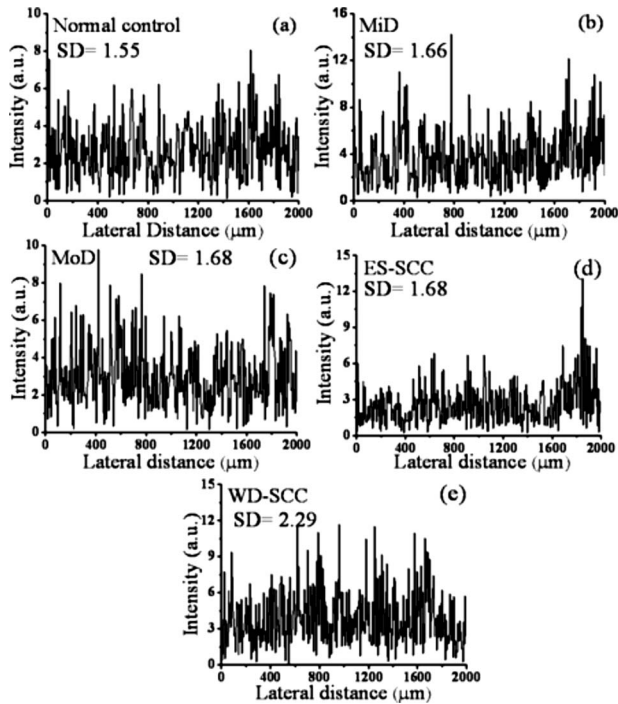
Fig. 3 (a)–(e) SS-OCT lateral scan profiles along the dashed lines in Figs. 2(a)–2(e) for the corresponding oral mucosal conditions. Their SD values are shown in the individual figures.
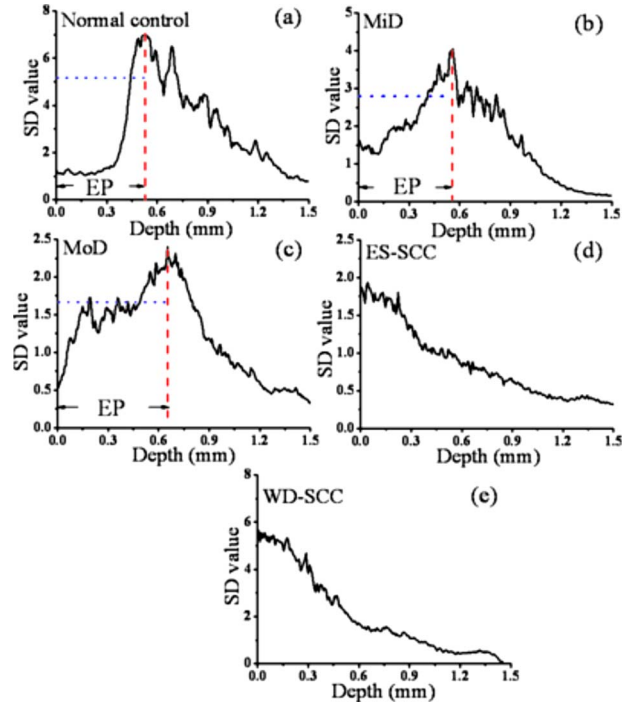
Fig. 4 (a)–(e) Depth-dependent SD values in the individual lateral scan ranges shown in Figs. 2(a)–2(e) for various oral lesion conditions.

by the arrows, correspond to the blood vessels. In each part of Fig. 2, a thin bright stripe at the top corresponding to the used plastic plate (PP) can be seen. In the SS-OCT images of the MiD [Fig. 2(b)] and MoD lesions [Fig. 2(c)], the EP and LP layers can still be distinguished and the EP thickness generally becomes larger. Then, in the images of ES-SCC [Fig. 2(d)] and WD-SCC [Fig. 2(d)], the boundaries between the EP and LP layers disappear. In the ES-SCC image, many vertical dark stripes, which are randomly arranged among vertical white bands, can be observed. It is believed that most of them correspond to the slitlike CTPs among epithelial ridges or among cancer cell nests. The CTP number becomes lower in the WD-SCC image. The lateral dashed lines of ~2 mm in length and 350 μm in depth indicate the lateral scan profiles for detailed analysis. The dashed lines are plotted following the variations of mucosal surfaces in SS-OCT scanning. Throughout this paper, the SS-OCT feature calibration in the lateral dimension is performed along a line of the same distance from the mucosal surface. Such calibrations will lead to the depth-dependent characteristics of the mucosa features. In each of Figs. 2(d) and 2(e) for the ES-SCC and WD-SCC cases, respectively, a rectangular area surrounded by dashed lines is chosen for detailed analysis, leading to the results to be shown later in Figs. 7 and 8.

Figures 3(a)–3(e) show the SS-OCT scan profiles along the dashed lines in Figs. 2(a)–2(e) for the corresponding oral mucosa conditions. Their SD values are shown in the individual figures. Here, at this particular depth (350 μm), it is difficult to find a variation trend among different oral lesion conditions. In Figs. 4(a)–4(e), we show the depth-dependent SD values in the individual lateral scan ranges shown in Figs. 2(a)–2(e) for various oral lesion conditions. Here, in each of
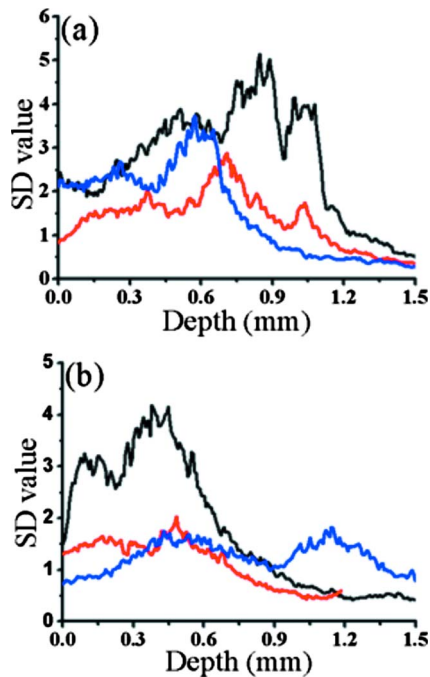
Fig. 5 Depth-dependent SD data of (a) another three oral MiD samples and (b) another three oral MoD samples.

Table 1 Percentage of the EP layer range, in which the SD value of lateral variation is >70%, the SD maximum in depth-dependent variation, of four MiD samples and four MoD samples.
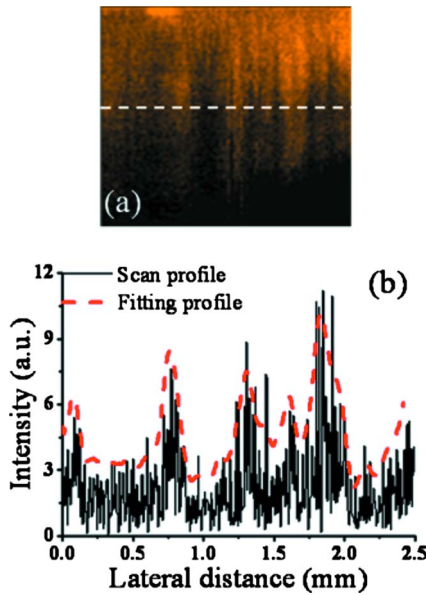
	Sample 1 (%)	Sample 2 (%)	Sample 3 (%)	Sample 4 (%)
MiD	30	47	47	56
MoD	71	83	86	72

from the conventional classification rule based on histology images, as discussed in Sec. 1. To further demonstrate this consistency, we show the depth-dependent SD data of another three MiD samples in Fig. 5(a) and another three MoD samples in Fig. 5(b). The evaluated percentage values of a relatively high SD level in the EP layer (>70% the individual maximum) of the four MiD and four MoD cases are shown in Table 1. Here, one can see that most of the evaluated percentage values of high SD level are larger than the definition ranges of MiD (0–33%) and MoD (33–67%). Such differences can be due to the assignment of the depth of SD maximum for the EP/LP boundary such that a 14% depth range of high SD exists in the normal control case. If the EP/LP boundary is redefined as the depth of SD rising point and a 14% or more can be subtracted from the values given in Table 1, then the results will be more consistent with the definition ranges.

On the other hand, in Figs. 4(d) and 4(e) for the cases of ES-SCC and WD-SCC, respectively, the SD maxima are shifted to the mucosa surfaces. In these two cases, SD values generally decrease monotonically along depth. By comparing Figs. 4(d) and 4(e) to Figs. 4(a)–4(c), one can clearly differentiate the stages of ES-SCC and WD-SCC from those of normal, MiD, and MoD. Also, by calculating the depth range of large SD value (relative to a designated level) above the EP/LP boundary, one can differentiate different stages of dysplasia. Nevertheless, based on the depth-dependent SD data, it is difficult to differentiate WD-SCC from ES-SCC. Other parameters are needed for such differentiation.

5 Indicators for the Differentiation between Different SCC Stages

To differentiate WD-SCC from ES-SCC, in Figs. 6(a) and 7(a), we show the SS-OCT images surrounded by the dashed lines in Figs. 2(d) and 2(e), respectively. The lateral scan intensity profiles indicated by the dashed lines in Figs. 6(a) and 7(a) are shown with the solid curves in Figs. 6(b) and 7(b), respectively. In either Fig. 6(b) or 7(b), we also plot a fitting profile by using the moving average method in the spatial-frequency spectrum.[26] Such a fitting profile well describes the features of the vertical dark stripes shown in Figs. 2(d) and 2(e) for the ES-SCC and WD-SCC cases, respectively. Most of those vertical dark stripes are believed to correspond to the CTP formed when a lesion evolves from the dysplasia stage into the SCC stage. In particular, with the features of CTP, the OCT intensity contrast along a lateral scan is expected to be stronger, compared to other features because CTP has very weak light scattering. Therefore, the fluctuation degree of such a fitting profile in either Fig. 6(b) or 7(b) can be used as

Figs. 4(a)–4(c), the maximum SD value roughly indicates the depth of the basement membrane (i.e., the boundary between the EP and LP layers). The maximum SD value in each case is obtained because of the variation of EP thickness along the lateral dimension. When a lateral scan profile of a fixed depth, as shown in Figs. 3(a)–3(c), is plotted, it passes through the EP and LP regions alternatively of different scattering intensities such that the fluctuation of OCT signal intensity is strong and the SD value is large. Because such a strong lateral intensity fluctuation exists in a depth range, the hump containing the SD maximum is generally quite broad. For convenience in analysis, in the following, the depth of SD maximum is designated as the boundary between the EP and LP layers. By comparing the depth-dependent SD variations between Figs. 4(a)–4(c), one can clearly see that the EP layer becomes thicker and thicker when the mucosa condition evolves from normal to MiD, then to MoD. Also, the range of relatively large SD value in the EP layer extended from the EP/LP boundary becomes larger and larger along the lesion deterioration process. For instance, in the normal control case, the SD maximum is located at 0.518 mm in depth. On the EP side, the depth range, in which the SD value is >70% the maximum value, is 0.073 mm, corresponding 14% EP thickness. Then, in the MiD (MoD) case, the SD maximum is located at 0.56 (0.651) mm in depth. On the EP side, the SD value drops to 70%, the maximum level at around 0.392 (0.189) mm in depth, corresponding to 30 (71)% EP thickness. The evaluation of the depth range of >70%, the SD maximum, is performed by searching upward from the SD maximum position for a depth, at which the SD value is 70%, the maximum, above which the SD value is always lower than the 70% maximum. Such percentage values of EP thickness for the MiD and MoD cases are generally larger than those

Fig. 6 (a) SS-OCT image surrounded by the dashed lines in Fig. 2(d); (b) lateral scan intensity profile (solid curve) indicated by the dashed line in (a). A fitting profile (dashed curve) is plotted in (b) with the moving average method in the spatial-frequency spectrum.

an important indicator for differentiating ES-SCC from WD-SCC. A higher CTP density in the stage of ES-SCC will make the fluctuation stronger. By comparing Fig. 6(b) to 7(b), one can indeed observe a stronger fluctuation in the fitting profile of the ES-SCC case. In Fig. 8, we show the zero-mean fitting profiles of four ES-SCC cases (solid curves) and four WD-SCC cases (dashed curves), including the cases in Figs. 6 and 7. Here, one can clearly see that, generally, the fluctuations of
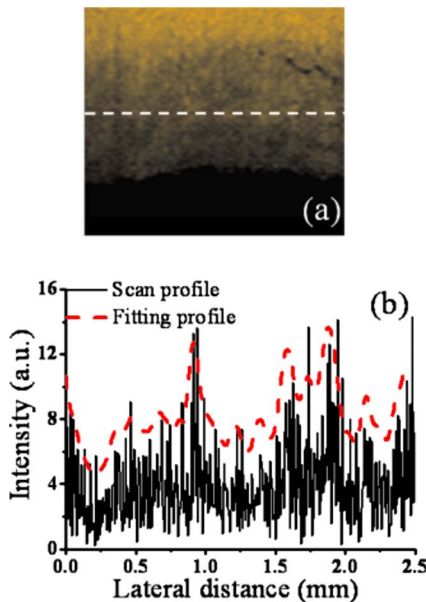
Fig. 7 (a) SS-OCT image surrounded by the dashed lines in Fig. 2(e); (b) lateral scan intensity profile (solid curve) indicated by the dashed line in (a). A fitting profile (dashed curve) is plotted in (b) with the moving average method in the spatial-frequency spectrum.
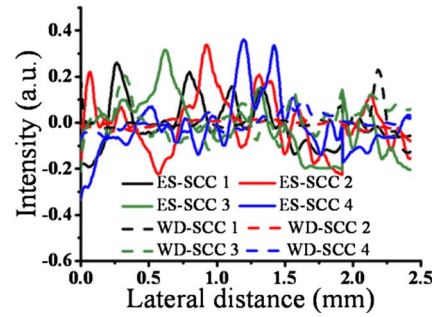

Fig. 8 Zero-mean fitting profiles in the lateral dimension of four ES-SCC cases (solid curves) and four WD-SCC cases (dashed curves).

the ES-SCC cases are stronger than those of the WD-SCC cases. The SD values of those zero-mean fitting profiles are shown in Table 2. Here, one can see that the SD values of the ES-SCC cases are significantly larger than those of the WD-SCC cases. Such an SD value can be an effective diagnosis indicator for differentiating ES-SCC from WD-SCC.

Another effective diagnosis indicator for differentiating ES-SCC from WD-SCC is the exponential decay constant of an averaged A-mode scan profile. During the stage of WD-SCC, the mucosa of the SS-OCT scanning depth range is filled with cancerous cells. In this situation, the density of blood capillary is expected to become higher in tissue such that light absorption is increased.[27] Therefore, the SS-OCT signal decays faster along depth. In Figs. 9(a) and 9(b), we show the A-mode scan profiles (solid curves), averaged over a B-mode scan range of 100 μm, of the ES-SCC and WD-SCC cases, respectively. Here, we also show the exponential decay fitting curves (dashed curves). The decay constant, α, values are given in the individual figures showing that the α value of 0.009 μm^{-1} in the ES-SCC case is significantly smaller than that of 0.015 μm^{-1} in the WD-SCC case. Figure 10 shows the α variations with lateral distance of four ES-SCC samples (solid curves) and four WD-SCC cases (dashed curves). Here, one can clearly see the differences between the ES-SCC and WD-SCC conditions. In Table 3, we show the values, averaged over the whole 2.5-mm lateral range, of the four ES-SCC and four WD-SCC samples. The average α values of the ES-SCC samples are significantly smaller than those of the WD-SCC samples. If we choose $\alpha = 0.012$ μm^{-1} as a criterion, the differentiation accuracy between ES-SCC and WD-SCC can be 100% among the eight samples used. Therefore, the exponential decay constant α can be an effective diagnosis indicator for differentiating ES-SCC from WD-SCC.

Table 2 SD values of the slowly varying lateral scan profiles in the four ES-SCC and four WD-SCC samples. The SD values of the ES-SCC cases are significantly larger than those of the WD-SCC cases.
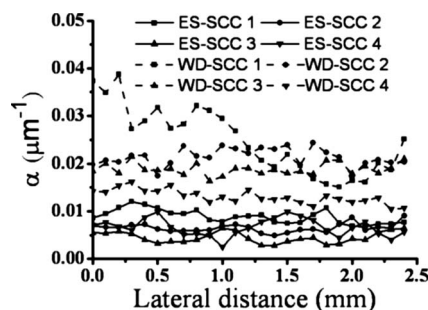
	Sample 1	Sample 2	Sample 3	Sample 4
ES-SCC	0.102	0.127	0.12	0.125
WD-SCC	0.047	0.019	0.071	0.035
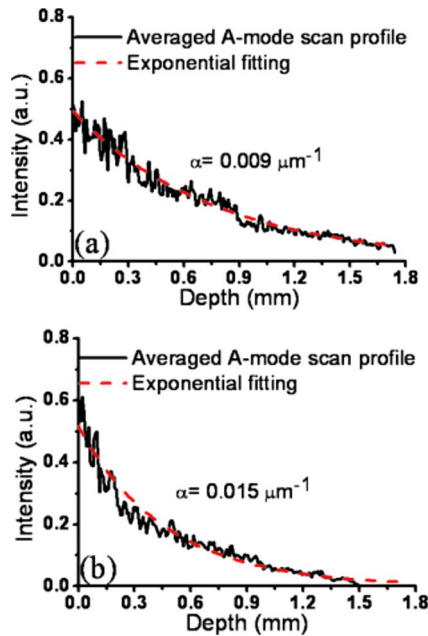
Fig. 9 A-mode scan profiles (solid curves), averaged over a lateral scan range of 100 μm, of the (a) ES-SCC and (b) WD-SCC cases. The exponential decay fitting curves (dashed curves) are also shown. The decay constant, α, values are indicated.

Table 3 α values, averaged over the 2.5-mm lateral distance in Fig. 10, of the four ES-SCC samples and four WD-SCC samples.

	Sample 1 (μm^{-1})	Sample 2 (μm^{-1})	Sample 3 (μm^{-1})	Sample 4 (μm^{-1})
ES-SCC	0.0088	0.0065	0.0045	0.0066
WD-SCC	0.0249	0.0213	0.0189	0.0131

evaluating SD values. Because of the higher CTP density in the ES-SCC stage, the SD values in the ES-SCC samples were significantly larger than those in the WD-SCC samples. Also, we used the exponential decay constant of an averaged A-mode scan profile to differentiate ES-SCC from WD-SCC. Because of the higher tissue absorption in the WD-SCC lesion, the decay constants in the WD-SCC samples were significantly larger than those in the ES-SCC samples. Because only several samples are collected thus far, a statistical analysis for evaluating sensitivity or specificity is still difficult. However, the clear differences of the used indicators between various lesion stages guarantee the usefulness of the proposed diagnosis technique based on SS-OCT scanning.

Acknowledgments

6 Conclusions

In summary, we have used an SS-OCT system to clinically scan oral precancer and cancer patients of various evolution stages, including normal control, MiD, MoD, ES-SCC, and WD-SCC, for diagnosis purpose. On the basis of the analyses of the SS-OCT images, we could differentiate the stages of dysplasia (MiD and MoD) and SCC (ES-SCC and WD-SCC) from normal control by evaluating the depth-dependent SD values of lateral variations. In the dysplasia stages, the boundary between the EP and LP layers could still be identified and the EP layer became significantly thicker than that of the normal control. Also, in a certain range of the EP layer above the EP/LP boundary, the SD value became larger than a certain percentage of the maximum level, which was observed around the EP/LP boundary. On the other hand, in the ES-SCC and WD-SCC stages, the EP/LP boundary disappeared. To differentiate ES-SCC from WD-SCC based on SS-OCT scanning, we used the slowly varying lateral scan profiles for

References

1. B. W. Neville, D. D. Damm, C. M. Allen, and J. E. Bouquot, "Epithelial pathology," in *Oral Maxillofacial Pathology*, pp. 259–321, W. B. Sauders, Philadelphia (1995).
2. D. M. Parkin, F. Bray, J. Ferlay, and P. Pisani, "Global cancerstatistics, 2002," *Ca-Cancer J. Clin.* **55**, 74–108 (2005).
3. M. Lingen, E. M. Sturgis, and M. S. Kies, "Squamous cell carcinoma of the head and neck in nonsmokers: clinical and biologic characteristics and implications for management," *Curr. Opin. Oncol.* **13**, 176–182 (2001).
4. Y. K. Chen, H. C. Huang, L. M. Lin, and C. C. Lin, "Primary oral squamous cell carcinoma: An analysis of 703 cases in southern Taiwan," *Oral Oncol.* **35**, 173–179 (1999).
5. A. Jemal, T. Murray, E. Ward, A. Samuels, R. C. Tiwari, A. Ghafoor, E. J. Feuer, and M. J. Thun, "Cancer statistics, 2005," *Ca-Cancer J. Clin.* **55**, 10–30 (2005).
6. B. W. Colston, Jr., M. J. Everett, L. B. Da Silva, L. L. Otis, P. Stroeve, and H. Nathel, "Imaging of hard- and soft-tissue structure in the oral cavity by optical coherence tomography," *Appl. Opt.* **37**, 3582–3585 (1998).
7. D. Huang, E. A. Swanson, C. P. Lin, J. S. Schuman, W. G. Stinson, W. Chang, M. R. Hee, T. Flotte, K. Gregory, C. A. Puliafito, and J. G. Fujimoto, "Optical coherence tomography," *Science* **254**, 1178–1188 (1991).
8. J. G. Fujimoto, M. E. Brezinski, G. T. Tearney, S. A. Boppart, B. E. Bouma, M. R. Hee, J. F. Southern, and E. A. Swanson, "Biomedical imaging and optical biopsy using optical coherence tomography," *Nat. Med. (N.Y.)* **1**, 970–972 (1995).
9. D. C. Adler, Y. Chen, R. Huber, J. Schmitt, J. Connolly, and J. G. Fujimoto, "Three-dimensional endomicroscopy using optical coherence tomography," *Nature Photon.* **1**, 709–716 (2007).
10. B. W. Colston, Jr., M. J. Everett, U. S. Sathyam, L. B. DaSilva, and L. L. Otis, "Imaging of the oral cavity using optical coherence tomography," *Monogr. Oral Sci. Rev.* **17**, 32–55 (2000).
11. L. L. Otis, M. J. Everett, U. S. Sathyam, and B. W. Colston, Jr., "Optical coherence tomography: a new imaging technology for dentistry," *J. Am. Dent. Assoc.* **131**, 511–514 (2000).

Fig. 10 α value variations along lateral distance of four ES-SCC samples (solid curves) and four WD-SCC cases (dashed curves).

12. E. Matheny, N. Hanna, W. Jung, Z. Chen, and P. Wilder-Smith, "Optical coherence tomography of malignancy in hamster cheek pouches," *J. Biomed. Opt.* **9**, 978–981 (2004).
13. P. Wilder-Smith, W. G. Jung, M. Brenner, K. Osann, H. Beydoun, D. Messadi, and Z. Chen, "*In vivo* optical coherence tomography for the diagnosis of oral malignancy," *Lasers Surg. Med.* **35**, 269–275 (2004).
14. A. L. Clark, A. Gillenwater, R. Alizadeh-Naderi, A. K. El-Naggar, and R. Richards-Kortum, "Detection and diagnosis of oral neoplasia with an optical coherence microscope," *J. Biomed. Opt.* **9**, 1271–1280 (2004).
15. W. Jung, J. Zhang, J. Chung, P. Wilder-Smith, M. Brenner, J. S. Nelson, and Z. Chen, "Advances in oral cancer detection using optical coherence tomography," *IEEE J. Sel. Top. Quantum Electron.* **11**, 811–817 (2005).
16. N. M. Hanna, W. Waite, K. Taylor, W. G. Jung, D. Mukai, E. Matheny, K. Kreuter, P. Wilder-Smith, M. Brenner, and Z. Chen, "Feasibility of three-dimensional optical coherence tomography and optical Doppler tomography of malignancy in hamster cheek pouches," *Photomed. Laser Surg.* **24**, 402–409 (2006).
17. J. M. Ridgway, W. B. Armstrong, S. Guo, U. Mahmood, J. Su, R. P. Jackson, T. Shibuya, R. L. Crumley, M. Gu, Z. Chen, and B. J. Wong, "*In vivo* optical coherence tomography of the human oral cavity and oropharynx," *Arch. Otolaryngol. Head Neck Surg.* **132**, 1074–1081 (2006).
18. B. Wong, R. Jackson, S. Guo, J. Ridgway, U. Mahmood, J. Shu, T. Shibuya, R. Crumley, M. Gu, W. Armstrong, and Z. Chen, "*In vivo* optical coherence tomography of the human larynx: normative and benign pathology in 82 patients," *Laryngoscope* **115**, 1904–1911 (2005).
19. W. Armstrong, J. Ridgway, D. Vokes, S. Guo, J. Perez, R. Jackson, M. Gu, J. Su, R. Crumley, T. Shibuya, U. Mahmood, Z. Chen, and B. Wong, "Optical coherence tomography of laryngeal cancer," *Laryngoscope* **116**, 1107–1113 (2006).
20. T. M. Muanza, A. P. Cotrim, M. McAuliffe, A. L. Sowers, B. J. Baum, J. A. Cook, F. Feldchtein, P. Amazeen, C. N. Coleman, and J. B. Mitchell, "Evaluation of radiation-induced oral mucositis by optical coherence tomography," *Clin. Cancer Res.* **11**, 5121 (2005).
21. P. Wilder-Smith, M. J. Hammer-Wilson, J. Zhang, Q. Wang, K. Osann, Z. Chen, H. Wigdor, J. Schwartz, and J. Epstein "*In vivo* imaging of oral mucositis in an animal model using optical coherence tomography and optical Doppler tomography," *Clin. Cancer Res.* **13**, 2449–2454 (2007).
22. M. T. Tsai, H. C. Lee, C. W. Lu, Y. M. Wang, C. K. Lee, C. C. Yang, and C. P. Chiang, "Delineation of an oral cancer lesion with swept-source optical coherence tomography," *J. Biomed. Opt.* **13**, 044012 (2008).
23. M. T. Tsai, H. C. Lee, C. K. Lee, C. H. Yu, H. M. Chen, C. P. Chiang, C. C. Chang, Y. M. Wang, and C. C. Yang, "Effective indicators for diagnosis of oral cancer using optical coherence tomography," *Opt. Express* **16**, 15847–15862 (2008).
24. P. R. Murti, R. B. Bhonsle, P. C. Gupta, D. K. Daftary, J. J. Pindborg, and F. S. Mehta, "Etiology of oral submucous fibrosis with special reference to the role of areca nut chewing," *J. Oral Pathol. Med.* **24**, 145–152 (1995).
25. N. Shah and P. P. Sharma, "Role of chewing and smoking habits in the etiology of oral submucous fibrosis (OSF): a case-control study," *J. Oral Pathol. Med.* **27**, 475–479 (1998).
26. J. H. McClellan, R. W. Schafer, and M. A. Yoder, *Signal Processing First*, Chap. 5, Pearson Education, Inc., Upper Saddle River, NJ (2003).
27. D. M. Brizel, S. P. Scully, J. M. Harrelson, L. J. Layfield, J. M. Bean, L. R. Prosnitz, and M. W. Dewhirst, "Tumor oxygenation predicts for the likelihood of distant metastases in human soft tissue sarcoma," *Cancer Res.* **56**, 941–943 (1996).